ASME Journal of Engineering for Gas Turbines and Power
Online journal at:
https://asmedigitalcollection.asme.org/gasturbinespower

G. Lemmi[1]
Department of Industrial Engineering,
University of Florence,
Via S.Marta 3,
Florence 50139, Italy
e-mail: gianmarco.lemmi@unifi.it

S. Castellani
Department of Industrial Engineering,
University of Florence,
Via S.Marta 3,
Florence 50139, Italy
e-mail: simone.castellani@unifi.it

S. Galeotti
Department of Industrial Engineering,
University of Florence,
Via S.Marta 3,
Florence 50139, Italy
e-mail: sofia.galeotti@unifi.it

A. Picchi
Department of Industrial Engineering,
University of Florence,
Via S.Marta 3,
Florence 50139, Italy
e-mail: alessio.picchi@unifi.it

R. Becchi
Department of Industrial Engineering,
University of Florence,
Via S.Marta 3,
Florence 50139, Italy
e-mail: riccardo.becchi@unifi.it

A. Andreini
Department of Industrial Engineering,
University of Florence,
Via S.Marta 3,
Florence 50139, Italy
e-mail: antonio.andreini@unifi.it

R. Meloni
Baker Hughes,
Via F. Matteucci 2,
Florence 50127, Italy
e-mail: roberto.meloni@bakerhughes.com

G. Babazzi
Baker Hughes,
Via F. Matteucci 2,
Florence 50127, Italy
e-mail: Giulia.Babazzi@bakerhughes.com

Prediction of the Flame Characteristics of an Industrial Gas Turbine Operated With CO_2-Diluted Air Through a High-Fidelity Numerical Analysis: A Comparison Between Flamelet Generated Manifolds and Artificially Thickened Flame

In light of the global commitment to decarbonize industrial processes, carbon capture and storage (CCS) plays a pivotal role in mitigating greenhouse gas emissions from gas turbine (GT) power generation processes. Achieving an efficient GT–CCS coupling requires the employment of high percentages of exhaust gas recirculation (EGR) to maximize the CO_2 content at the CCS inlet. Nevertheless, such operating conditions pose critical challenges for conventional combustion systems due to reduced oxygen levels associated with higher EGR, limiting engine operability. To address this challenge, the development of innovative technical solutions is essential to extend the combustor operational capabilities at high EGR rates. For this goal, a significant number of computational fluid dynamics (CFD) simulations are required to identify the flame stability limits across various EGR levels and burner designs. It is imperative, in this context, to minimize computational costs while maintaining high accuracy. In this work, a comprehensive comparative study of an extended version of the flamelet generated manifolds (FGM) and the artificially thickened flame (ATF) model is performed through a large eddy simulation (LES)-based CFD analysis. The investigation is performed within the context of an industrial lean-premixed burner manufactured by Baker Hughes, operating with natural gas and CO_2-diluted air at atmospheric pressure. While the extended-FGM has been previously presented by the authors in a study on the same test rig under standard air conditions, the current work aims to extend its application to critical oxygen-depleted conditions, where near-blowout phenomena such as flame liftoff and length elongation may become significantly pronounced. Numerical validation is carried out through a direct comparison of the computed averaged heat release, representing the flame topology, with detailed OH chemiluminescence images from a test campaign conducted by the technology for high temperature (THT) Lab of the University of Florence. The experimental data will serve as the primary benchmark for assessing the models' effectiveness in capturing the main dynamics of such critical operating conditions. Furthermore, potential disparities in both thermal and flow fields at the burner exit region between the two models will be discussed.* [DOI: 10.1115/1.4066510]

Turbo Expo, June 24–28, 2024. GT2024.
[1]Corresponding author.
Manuscript received July 9, 2024; final manuscript received July 16, 2024; published online October 15, 2024. Editor: Jerzy T. Sawicki.

1 Introduction

In the context of the global shift toward sustainable and low-impact renewable energy [1], the imperative to transition from conventional fossil fuels to carbon-free alternatives is paramount. This transition is a fundamental response to the urgent challenges of climate change, air pollution, and the need for energy systems with reduced carbon footprints. In the pursuit of decarbonization [2], exploring carbon-free fuels, with hydrogen emerging as a leading solution, becomes crucial [3]. However, given the current limited availability of carbon-free fuels, the quest for flexible and immediate temporary technical solutions is of utmost importance [4]. These solutions aim to enable the simultaneous use of both conventional and carbon-free fuels, with the ultimate goal of minimizing CO_2 and NO_x pollutant emissions. From the perspective of the power generation sector, the integration of carbon capture and storage (CCS) systems holds promise for mitigating CO_2 emissions from gas turbines (GT) [5]. To ensure an efficient and cost-effective coupling between the gas turbine system and the CCS process, it is mandatory to employ an extremely high percentage of exhaust gas recirculation (EGR), capable of maximizing the CO_2 content at the inlet of the carbon capture unit [6–10]. However, it is noteworthy that such operating conditions are surely detrimental to conventional combustion systems since the increase in the EGR level limits the operability range of the engine. Indeed, EGR alters the fresh mixture composition, leading to a CO_2 and N_2 enrichment of the oxidizer. From the flame reactivity perspective, the effects of CO_2 dilution in laminar conditions have been widely investigated by Xie et al. [11]. Their findings indicate that the addition of CO_2 contributes to a decrease in reactivity through different pathways (…). Because of that, in a turbulent combustion scenario, achieving flame stabilization at high EGR levels poses a significant challenge. In this context, De Persis et al. [12] conducted experimental investigations on the effects of CO_2 addition on the flame stability of a perfectly premixed swirl-stabilized test case, reaching CO_2 concentrations associated with the blowout limit. While this study provides an initial sensitivity assessment to the effects of CO_2 addition, the simplistic design of the burner does not yield relevant information for enhancing flame stability.

Overcoming this challenge necessitates the creation of cutting-edge technical solutions to broaden the operational capabilities of the combustor under high EGR rates. To achieve this objective, computational fluid dynamics (CFD) could play a crucial role by pinpointing flame stability limits across various EGR levels and burner configurations, thus speeding up the design phase of novel technical solutions. Therefore, from the industrial sector standpoint, it is essential to employ models capable of accurately addressing near-blowout phenomena such as flame liftoff and length elongation, typical of such critical operating conditions. On the other side, the design phase requires an extensive series of CFD simulations in order to assess the impact of different technical solutions on the flame stability limits under specific EGR levels, emphasizing the need to effectively manage the computational cost.

In the realm of large eddy simulation (LES) applications to GT-combustors, two turbulent combustion model approaches take center stage in the technical literature: on one front stands the species transport formulation, prominently represented by the widely recognized artificially thickened flame (ATF) model, especially from an academic standpoint, which directly solves a transport equation for each species involved in the employed reaction mechanism; on the other side, the tabulated-chemistry approach, with the flamelet generated manifold (FGM) model standing as the pre-eminent choice. Here, a look-up table is pregenerated through a detailed reaction mechanism as a function of a limited set of control variables, containing all thermodynamic quantities. The table is then queried at runtime based on the solution of a limited set of control variables' transport equations. While the FGM is extensively employed for its computational efficiency, it lacks direct consideration for critical physical factors such as stretch and heat loss phenomena. In contrast, the ATF naturally accommodates these effects, although at the expense of a significant increase in the overall computational cost of the simulation and its limitation to correctly handling perfectly premixed mixtures only.

In this study, enhanced versions of both ATF and FGM models are employed to address their inherent limitations. For the ATF, an upgraded iteration of the dynamic thickened flame model for large eddy simulations (DTFLES) [13,14] was employed to broaden its applicability to nonpremixed flames. This extension relies on a formulation that exploits a flame sensor which acts on the thickening factor by disabling it in the proximity of a diffusive flame front, thus allowing for spatial variations of combustion metrics to be properly accounted for [15]. As for the FGM, the turbulence–chemistry interaction is modeled through an extended version of the finite-rate approach that takes into account both stretch and heat loss effects [16,17].

The primary objective of the present LES-based CFD investigation is to comprehensively compare the turbulent combustion models mentioned above in predicting flame topology within the framework of an industrial GT lean-premixed combustor manufactured by Baker Hughes, specifically operated under high levels of CO_2 dilution. In a prior study by the authors [18], the two models were compared under standard air conditions, exhibiting a high degree of agreement with each other and a remarkable accuracy in predicting the flame topology. However, those operating conditions were characterized by low levels of both stretch and heat loss, which mitigated near-blowout phenomena such as flame liftoff and length elongation. Importantly, these phenomena, when present, may significantly amplify the differences between ATF and FGM, thus underscoring the need for a proper investigation. The current study aims to extend the assessment of those models' predictive capabilities in terms of flame topology by exploring highly CO_2-diluted air conditions, where the lack of oxygen concentrations poses critical challenges for both flame stabilization and the CFD modeling capabilities in accurately reproducing near-blowout phenomena.

The computational results provided by both the extended versions of the ATF and FGM models are compared to OH* chemiluminescence images obtained during an experimental campaign conducted in the reactive cell of the technology for high temperature (THT) Lab of the University of Florence. Section 2 will present details on the experimental test rig and the investigated operating conditions, followed by a description of the numerical modelling in Secs. 3 and 4. Subsequently, a comprehensive comparison of the two models will be presented, focusing on flame topology, thermal fields, and mixing fields.

2 Experimental Rig and Operating Conditions

Experiments and CFD simulations are conducted within the framework of a GT lean-premixed burner, engineered by Baker Hughes for heavy-duty applications. The burner is physically housed in an optically accessible reactive cell at the THT Lab of the University of Florence and is supplied through two independent fuel lines [19]. Figure 1 schematically illustrates the key features of the burner and the test rig itself. The assurance of an almost perfectly premixed air–fuel mixture at the chamber entrance is ensured by the presence of a double counter-rotating swirler, while flame stabilization is achieved through a series of diffusive piloted flames. The combustion chamber features an internal diameter of 110 mm and an axial extension spanning approximately 2.5 diameters, defining the principal geometric dimensions of this experimental setup.

The test rig operates with CO_2-diluted air preheated to 578 K as oxidizer, simulating the effects of an exhaust gas recirculation (EGR) integrated system, and natural gas as fuel, the latter with an inlet temperature of 291 K. All tests are conducted under standard ambient pressure conditions. A constant oxidizer mass flow rate is injected through the plenum, supplying both the burner and the ducts dedicated to cooling the liner. The total fuel mass flow rate is adjusted to attain a thermal power output of approximately 74 kW,

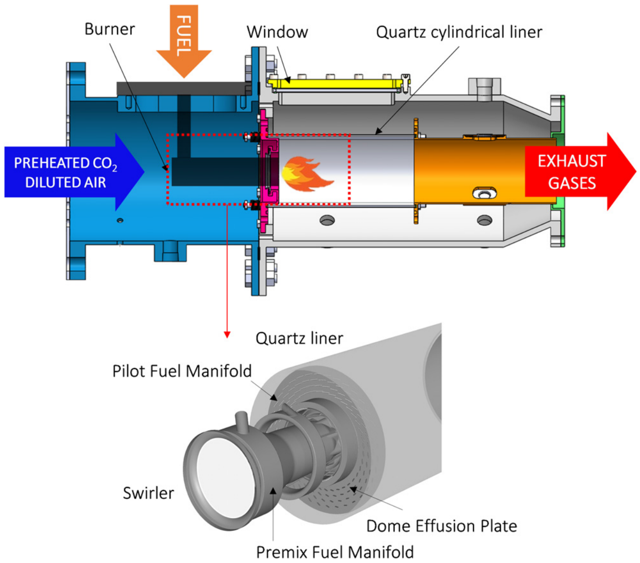

Fig. 1 Schematics of the THT Lab reactive test cell (top) [20] equipped with Baker Hughes lean-premixed burner (bottom)

with the pilot split set to 30%. A stable pressure drop ($\Delta P/P$) of around 4.2% was measured across the combustion chamber.

In terms of rig instrumentation, a HORIBA PG-350 was employed for analyzing the flue gas composition and retrieving key pollutant emissions such as CO and NO_x. A Phantom MIRO M340 camera was utilized for both particle image velocimetry investigations and OH* chemiluminescence measurements, the latter crucial for a proper assessment of the flame topology. Additional details regarding the test rig are available in the work of Babazzi et al. [20].

3 Numerical Setup

The numerical fluid domain includes the complete burner geometry, featuring a compressor discharge plenum, a double counter-rotating swirler, two fuel manifolds with respective pilot ducts, effusion holes, and all the other components characterizing the combustor. Figure 2 illustrates the computational mesh grid on a plane intersecting two axes of the pilot line. The domain consists of a fully unstructured mesh comprising approximately 20×10^6 polyhedral cells. Local mesh resolution enhancements, determined in prior sensitivity analyses by the authors—omitted here for brevity—are incorporated within the key zone regions of the burner to improve the prediction of the mixing process around the pilot jets, and to ensure an accurate resolution of the high turbulence levels generated by the swirler. The latter is crucial for a proper description of the diffusion process that the flow undergoes upon entering the combustor primary zone. The locally refined mesh sizings are reported in Fig. 2.

Simulations were conducted using the commercial pressure-based code ANSYS FLUENT 2022 R1. To resolve turbulence, an unsteady high-fidelity LES approach was employed, coupled with the wall-adapting local eddy-viscosity (WALE) subgrid scale model for addressing unresolved eddies. The preference for the WALE model over the previously employed [18] dynamic Smagorinsky–Lilly formulation [21], which dynamically evaluates the Smagorinsky constant, was motivated by its capability to accurately capture the correct wall asymptotic behavior for wall-bounded flows [22,23]. Given the complex double-swirler geometry of the burner under study, an accurate prediction of the flow near the swirler walls was deemed crucial for enhancing the overall accuracy of the flow field. The pressure–velocity coupling was handled by the pressure implicit with split operator algorithm [24,25], employing second-order schemes for both spatial discretization and transient

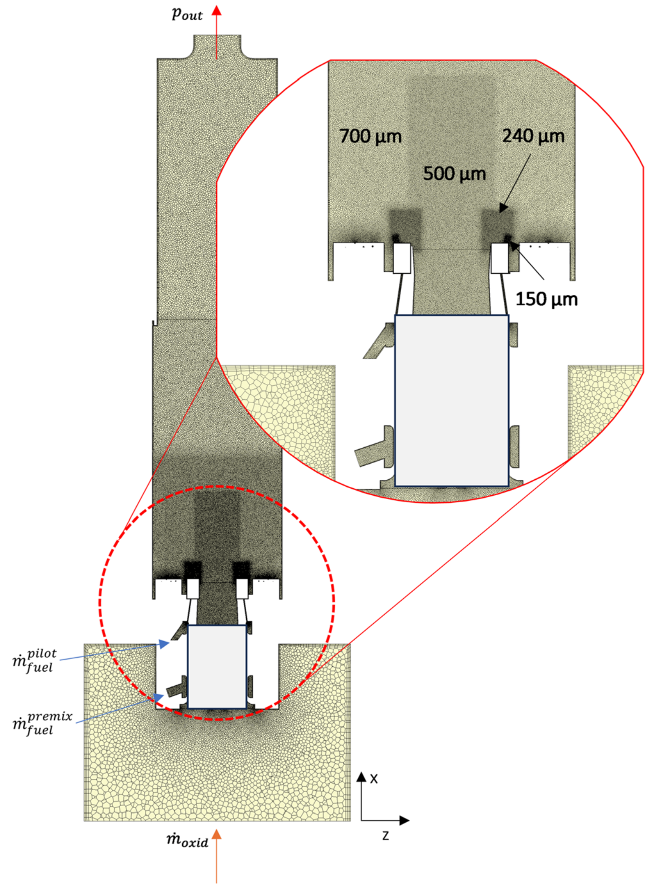

Fig. 2 Computational grid on a plane intersecting two axes of the pilot fuel line (midplane section). The mesh resolution is enhanced within the swirler and the primary zone regions, with its peak in the pilot fuel injection for a refined characterization of the mixing process. Design details omitted.

formulation, and a constant time-step of 5.0×10^{-6} s, thus ensuring a maximum Courant number of 8 within the pilot jets region.

Building upon the data presented in Sec. 2, a constant mass flow rate was assigned to both the oxidizer and fuel at their respective inlet patches, while the pressure-outlet boundary condition was set to match standard atmospheric conditions. A constant temperature boundary condition was imposed on the dome walls, while for the chamber and flame tube ones, a convective heat transfer thermal boundary condition was applied. The heat transfer coefficient (HTC) value was determined through a test campaign aimed at ensuring an accurate reproduction of the wall temperatures measured during the experiments.

4 Mathematical Formulations of the Tested Turbulent Combustion Models

4.1 Dynamic Thickened Flame Model for Large Eddy Simulations. The underlying principle of the ATF models family revolves around the assessment of turbulence–chemistry interaction through the artificial thickening of the unresolved flame. This approach aims to create a sufficiently thick flame brush that can be directly resolved within the given mesh sizing, thus avoiding the need for a specific subgrid model formulation. In this comprehensive comparison, the dynamic thickened flame model for LES [26] is employed to assess turbulence–chemistry interaction, utilizing the Colin et al. [27] formulation for the efficiency function. This ATF model version achieves flame thickening through the introduction of additional terms in both species mass fraction and energy transport equations, including the aforementioned efficiency function (E), a flame sensor (Ω), and a dynamic thickening factor (F), the latter representing the focal point of the present model. Unlike the original ATF version, which employs a constant value for F, a dynamic thickening factor is implemented, activating in the regions close to the flame front ($F < 1$) and deactivating away from the flame ($F = 1$). The thickening factor (F) modulation occurs through the exploitation of a sensor (Ω) based on an "Arrhenius-like" expression, not detailed here for brevity. According to the formulation by Legier et al. [28], the sensor (Ω) acts on the thickening factor as follows:

$$F = 1 + (F_{\max} - 1)\tanh\left(\beta \frac{\Omega}{\Omega_{\max}}\right) \tag{1}$$

Here, $\Omega_{\max}$ is the maximum value of Ω and can be analytically determined for a stoichiometric premixed flame. β is a parameter controlling the transition in flame thickness between regions where F is activated and not, while $F_{\max}$ is the local maximum thickening factor, computed as a function of the local mixture composition and mesh sizing (Δx)

$$F_{\max} = \frac{\Delta x N_{\mathrm{Thick}}}{D_{\mathrm{th}}} \tag{2}$$

Here, D_{th} stands for the thermal laminar flame thickness, which is tabulated as a function of the local mixture composition, and N_{Thick} represents the number of grid points within the laminar flame thickness.

In numerous gas turbine applications, burners employ injection strategies that result in flames exhibiting multiple combustion regimes, for which a careful selection of the proper turbulent combustion model becomes critical. The DTFLES model employed in this study follows the methodology outlined by Castellani et al. [14], where a flame index is implemented to discern between combustion regimes, enabling distinct modeling for premixed and diffusive combustion. Specifically, the Takeno flame index (ξ), defined by Yamashita et al. [29] as the normalized dot product of the gradients of the fuel and oxidizer mass fractions, is utilized

$$\xi = \frac{\nabla Y_{F,\max} \cdot \nabla Y_{O,\max}}{|\nabla Y_{F,\max} \cdot \nabla Y_{O,\max}|} \tag{3}$$

In the premixed combustion regime, where fuel and oxidizer gradients are aligned (resulting in a flame index of $+1$), Legier's formulation is applied, with the flame thickness discretized through ten mesh points. Conversely, in a diffusive regime where fuel and oxidizer gradients are not aligned (yielding a negative flame index), no flame front thickening is applied. Consequently, a finite-rate closure is adopted. Further insights into the Takeno index implementation can be found in the study conducted by Rosenberg et al. [30].

The same skeletal mechanism employed in previous work from the authors, consisting of 19 species and 62 reactions retrieved from the detailed U.C. San Diego mechanism [31], is utilized to minimize the computational cost of the DTFLES approach.

4.2 Flamelet Generated Manifold: Extended Finite-Rate.

The FGM method stands out as the most widely adopted turbulent combustion model within the flamelet concept category [32]. Typically, methodologies falling under this category framework rely on the assumption that the thermodynamic state of any point in the computational domain can be aptly described by two independent control variables, i.e., the mixture fraction (Z) and the reaction progress variable (c) [33]. In the FGM approach, several laminar flamelets are solved during the preprocessing stage to generate a look-up table containing all thermodynamic quantities ($T, Y_i, \dot{\omega}_c$, etc.) expressed solely as functions of the two aforementioned control variables. In this work, a 64×32 laminar flamelets database in the $Z \times c$ space is generated utilizing the comprehensive GRI-MECH 3.0 [34], which comprises 53 species and 325 elementary chemical reactions. Assuming statistical independence of the control variables' probability density function (PDF), the turbulence–chemistry interaction is accounted for by describing variables stochastically through the use of a joint mass-weighted β-shaped probability density function (β − PDF) of Z and c, $\tilde{P}(Z, c)$ [35]. A pre-integrated look-up table for turbulent combustion is then constructed by PDF-averaging the laminar flamelet database. These assumptions make the FGM a cost-effective and widely used solution for modeling turbulent combustion in industrial gas turbine applications.

The closure of the turbulent progress variable source term ($\tilde{\dot{\omega}}_c$) is performed through the employment of an extended version of the finite-rate (FR) approach. This enhancement takes into account flame stretch and heat loss effects through a precalculated table (Γ-table), thus promoting a reduction in the overall combustion process reactivity. This is achieved by defining a new correction factor (Γ), tabulated as a function of the mixture fraction (Z), strain rate (a), and heat loss (ψ), multiplying the standard finite-rate turbulent progress variable source term as follows:

$$\tilde{\dot{\omega}}_c(\tilde{Z}, \tilde{c}) = \Gamma(Z, a, \psi) \underbrace{\int\int \dot{\omega}_c(Z, c) P(Z, c)\, dZ\, dc}_{\text{Standard FR turbulent } c \text{ source term}} \tag{4}$$

With $\dot{\omega}_c$ directly extracted from the laminar flamelets' look-up table. $\Gamma(Z, a, \psi)$ is defined as the ratio between the maximum value of the strained, nonadiabatic progress variable source term and the adiabatic, unstrained one in a one-dimensional laminar flame

$$\Gamma(Z, a, \psi) = \frac{\max \dot{\omega}_c(Z, a, \psi)}{\max \dot{\omega}_c^0(Z)} \tag{5}$$

Here, ψ identifies the heat loss parameter, defined as the ratio between the burnt gas temperature and the corresponding equilibrium value, while a represents the strain, the latter computed through a set of quantities defining the velocity flow field. Several freely propagating flames ($a = 0$) and premixed counterflow flames ($a > 0$) are solved through CANTERA libraries to generate the $\Gamma(Z, a, \psi)$ table. In Fig. 3, the Γ table in Z and a space for the adiabatic condition ($\psi = 1$) is reported.

Transitioning from the preprocessing to the CFD processing stage, a user defined function (UDF) containing an analytical expression for stretch is employed within the solver. The formula expresses flame stretch (κ) as a combination of resolved strain ($\tilde{a}_{\mathrm{res}}$), subgrid scale strain ($\tilde{a}_{\mathrm{sgs}}$), and curvature (σ_c)

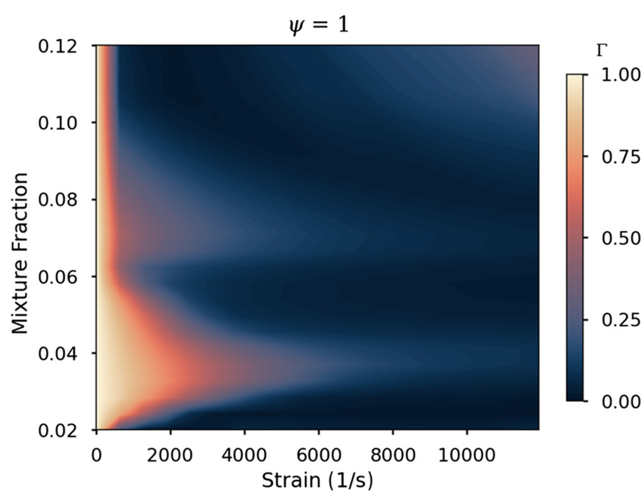

Fig. 3 Γ table in the mixture fraction and strain space for the adiabatic condition (ψ=1)

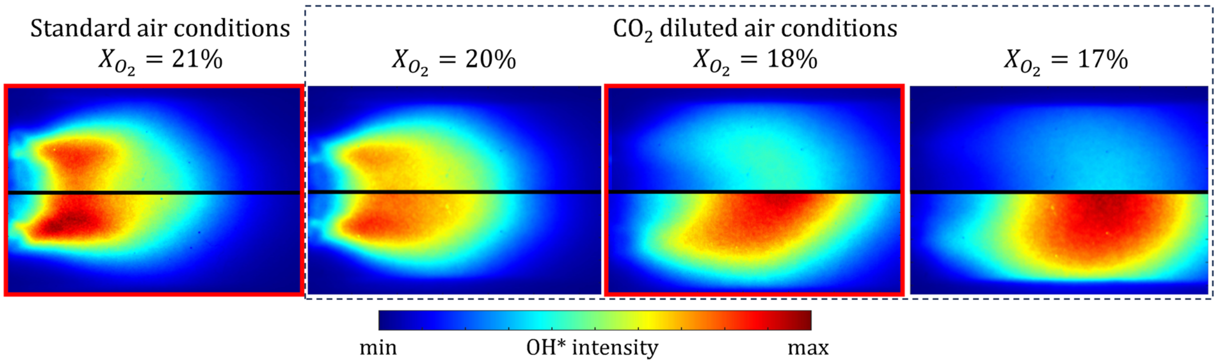

Fig. 4 Time-averaged OH* chemiluminescence images for standard (left) and different CO_2-diluted air levels conditions. Upper halves: absolute OH* intensity, lower halves: normalized with each own maximum. The outlined images represent cases simulated with CFD.

$$\kappa = \left(\delta_{ij} - \tilde{n}_i\tilde{n}_j\right)\frac{\partial \tilde{u}_i}{\partial x_j} + \Gamma_k \frac{\sqrt{k_{\text{sgs}}}}{\Delta} + S_l \frac{\partial \tilde{n}_i}{\partial x_i} = \tilde{a}_{\text{res}} + \tilde{a}_{\text{sgs}} + \sigma_c \quad (6)$$

In this equation, δ_{ij} is the Kronecker delta, n is the normal vector to the flame front, Γ_k is an efficiency function [36], k_{sgs} is the subgrid kinetic energy, and S_l is the laminar flame speed. It is essential to note that the influence of stretch on the flame front depends solely on the magnitude of the combined effects of strain and curvature, and the distribution of the two does not alter it. This allows for the use of strained flamelets—i.e., premixed counterflow flames—to serve as a representative for both strain and curvature in constructing the gamma table. Further insights into this advanced version of the FGM can be found in Refs. [16] and [17].

5 Results and Discussion

In this section, the main results of the high-fidelity CFD campaign performed on Baker Hughes' lean-premixed burner are presented.

The initial segment of this section offers a brief description of the CO_2 dilution effects on the flame topology through a comparison of experimental time-averaged OH* chemiluminescence images on the line of sight between standard and diluted air conditions. Subsequently, the influence of the chosen turbulent combustion model on the flame topology is discussed. Finally, an examination of thermal, mixing, and velocity fields within the chamber is provided. The time-averaged mean mixture fraction field serves as a valuable resource for comprehending the observed flame dynamics, highlighting the significance of CFD investigations in complementing experimental test campaigns.

5.1 Flame Topology. As mentioned earlier, the explored operating conditions involve a substantial level of CO_2 dilution within the oxidizer, leading to a pronounced deterioration of key parameters characterizing the combustion process, including the laminar flame speed. The introduction of CO_2-diluted air within the combustion chamber indeed results in a lower heat generation from the combustion process due to reduced oxygen concentration. Another consequential effect is attributed to the high specific heat capacity of the CO_2, which further reduces both the flame heat release and temperature. These effects have a direct impact on the flame topology. Figure 4 presents the time-averaged OH* chemiluminescence images for both standard (left) and CO_2 diluted (right) air conditions. The upper halves depict the absolute OH* intensity, while the lower halves report the normalized intensity, each with its own maximum. Three macroscopic effects are discernible: first, a reduction in the OH* signal intensity, a clear indicator of the reduced heat release attributed to the decreased oxygen concentration and the high specific heat of CO_2. Another notable phenomenon is the elongation of the flame length in the case of diluted air, deriving from the deterioration of the laminar flame speed. Finally, a local flame liftoff is observed around the pilot jets region. This specific phenomenon should be sought during the transient phase preceding the flame stabilization process. Experimental observations indicate a progressively increasing liftoff with higher levels of CO_2 dilution, stabilizing at a certain distance from the dome once the desired CO_2 dilution level is achieved.

From a turbulent combustion modeling standpoint, both the ATF and FGM effectively capture the reduction in heat release and flame length elongation, as depicted in Fig. 5. The figure displays normalized time-averaged heat-release contours on the burner midplane section from both models under standard and CO_2-diluted air conditions. Normalization is performed by utilizing the associated maximum time-averaged heat-release value from standard air conditions. While negligible differences in flame topology are observed under standard conditions, notable variations emerge under CO_2-diluted air conditions. Specifically, the FGM model exhibits a marginally more pronounced reduction in heat release compared to ATF. Additionally, the heat-release distribution slightly differs, as shown in Fig. 6, where normalized time-averaged heat-release contours from both models are compared to the normalized OH* signal from experimental tests. The ATF model

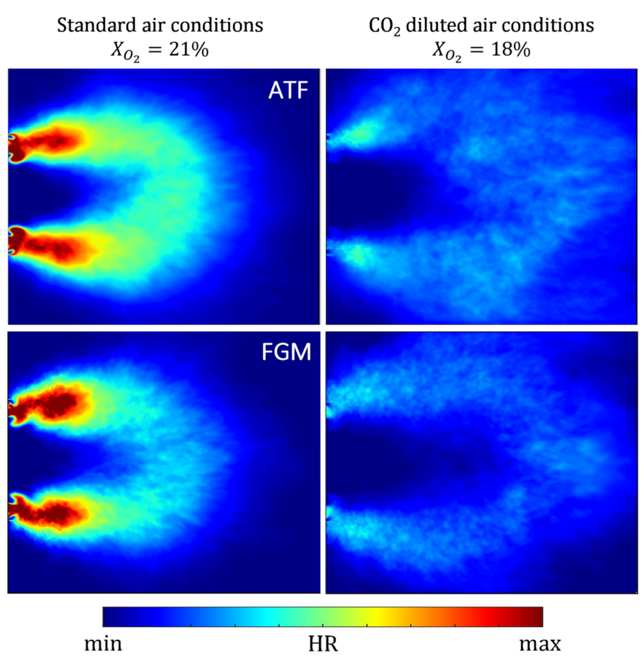

Fig. 5 Normalized time-averaged heat-release contours on the $z-x$ plane of symmetry of the burner from the ATF (top) and FGM (bottom) models for standard (left) and CO_2 diluted (right) air conditions

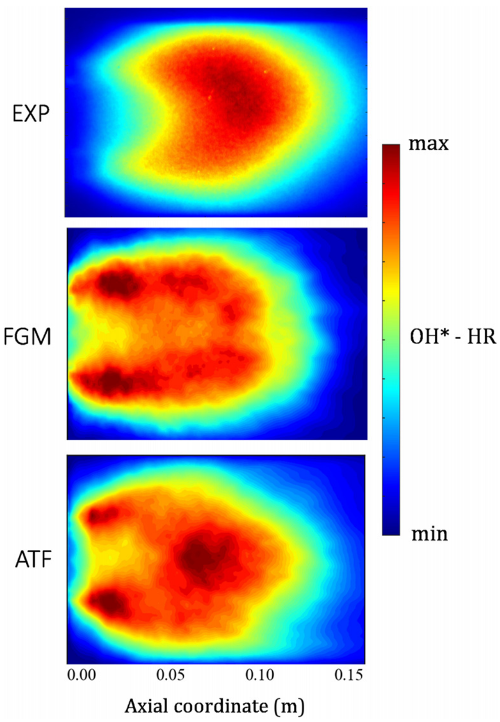

Fig. 6 Line of sight views of the normalized time-averaged heat-release contours from the FGM and ATF models compared with the normalized OH* signal from the experimental test campaign

appears to better predict the position of the heat-release peaks: one is situated on the symmetry axis of the flame, far away from the dome, consistent with the OH* map, while the second one is located around the pilot jets region, a phenomenon not observed in the experimental campaign. In contrast, the FGM positions the heat-release peak solely at the pilot jets exit, without being able to capture the central peak. No significant differences can be observed regarding the flame length, with both models capable of effectively capturing the elongation associated with the decrease in the laminar flame speed. It is noteworthy that neither model adequately captures the liftoff phenomenon, even if the ATF shows a slightly better performance associated with a decrease in heat release around the pilots exit region. This inability to properly capture the flame liftoff is consistent with the prior work by the author, even if the experimental liftoff under standard air conditions was less pronounced.

A preliminary analysis suggested that the inability to capture the local flame liftoff could be attributed to thermal boundaries. For this purpose, the presented study included an investigation of the influence of wall heat loss on flame topology. However, due to space constraints, detailed results of this sensitivity are not provided here. The analysis involved adjustments to the convective heat transfer thermal boundary condition on the flame-tube walls. Two distinct HTC values, leading to different wall temperature distributions, were tested to evaluate their impact on flame structure. Given the similarity in flame topology between the tested combustion models, this investigation was conducted exclusively on the FGM, considering its reduced computational cost. Interestingly, no significant differences were observed, as shown in Fig. 7. The flame retained the same stabilization mechanism, anchoring on the pilot jets, with minimal alterations in both flame length and heat-release magnitude distribution.

It is worth mentioning that, while the numerical simulations indicate a stable anchoring of the flame to the pilots, experimental observations reveal an unstable-rotating behavior of the flame following the ignition event. This discrepancy implies not only an inaccurate prediction of the flame topology but also a divergence in the stabilization dynamics from the experimental scenario. Since the ignition process is not simulated in the current study, the

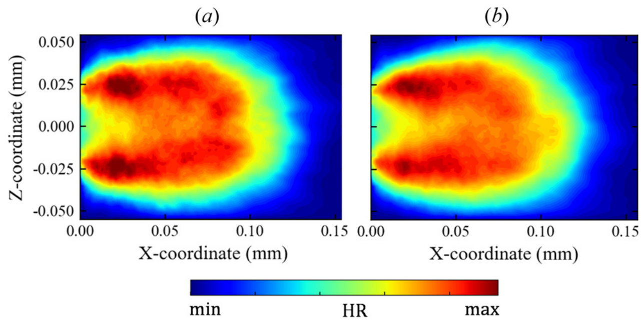

Fig. 7 Line of sight views of the normalized time-averaged heat-release contours from the FGM for two different wall thermal boundary HTC values: (*a*) $HTC_1/HTC_2 = 0.175$ and (*b*) $HTC_2/HTC_2 = 1$

aforementioned flame instability cannot be numerically captured. This suggests that the prediction of the local flame liftoff might be linked to a possible hysteresis in the flame stabilization dynamics associated with the transient phase following the ignition process. This emphasizes the need for further investigations to comprehensively understand and address those dynamics and disparities.

5.2 Thermal, Mixing, and Velocity Fields. In this section, the time-averaged static temperature, mixture fraction, and velocity magnitude fields within the chamber are examined.

In terms of mixing, the presence of a dual counterswirling premixer plays a crucial role in achieving a well-uniformed fuel–oxidizer mixture. Figure 8 shows the normalized time-averaged contours of mixture fraction as well as the corresponding root-mean-square error values on the domain midplane. The mixture fraction map at the premixer–chamber interface (section A–A) underscores the effectiveness of the employed premixer in achieving a well-mixed mixture in the primary zone. This effectiveness is further supported by the almost complete identification of a premixed flame regime, as determined by analyzing the Takeno flame index from the ATF model simulation. To illustrate, Fig. 9 presents the instantaneous map of the product between the normalized Takeno flame index and fuel consumption. Positive values indicate a premixed regime, while negative values are associated with a diffusive one. Although there is a localized region around the pilots characterized by a nonpremixed regime, the main flow coming from the swirler predominantly operates under premixed conditions.

A more detailed description of both mixing and velocity fields within half of the chamber domain is depicted in Fig. 10. The existence of an outer recirculation zone plays a crucial role in flame stabilization by contributing to the formation of the shear layer around the pilots and supplying them with hot exhaust gases. While exhaust gas recirculation generally supports flame stabilization, under heavily CO_2-diluted conditions, it might contribute to local flame liftoff due to reduced oxygen concentration. Furthermore, this dynamic scenario could pose challenges for the FGM compared to the ATF due to the inherent differences between a tabulated-chemistry approach and species transport, thus potentially justifying the FGM's marginal inferior flame topology prediction observed in the present study. A smaller recirculation zone is noticeable around the chamber corner region, attributed to the injection of effusion cooling jets. It is noteworthy that the cooling flow seems to act as a shield, preventing the more external recirculated gases, cooled by their interaction with the cold flame-tube walls, from directly impacting the pilot jets. This observation may partially justify the previous finding regarding the low impact of wall heat losses on the flame structure and raises the possibility that flame liftoff might be associated with dynamics such as the ignition transient phase rather than the thermal wall boundary conditions.

A comparative analysis of the ATF and FGM models, focusing on the mixing process, is illustrated in Fig. 11, where instantaneous

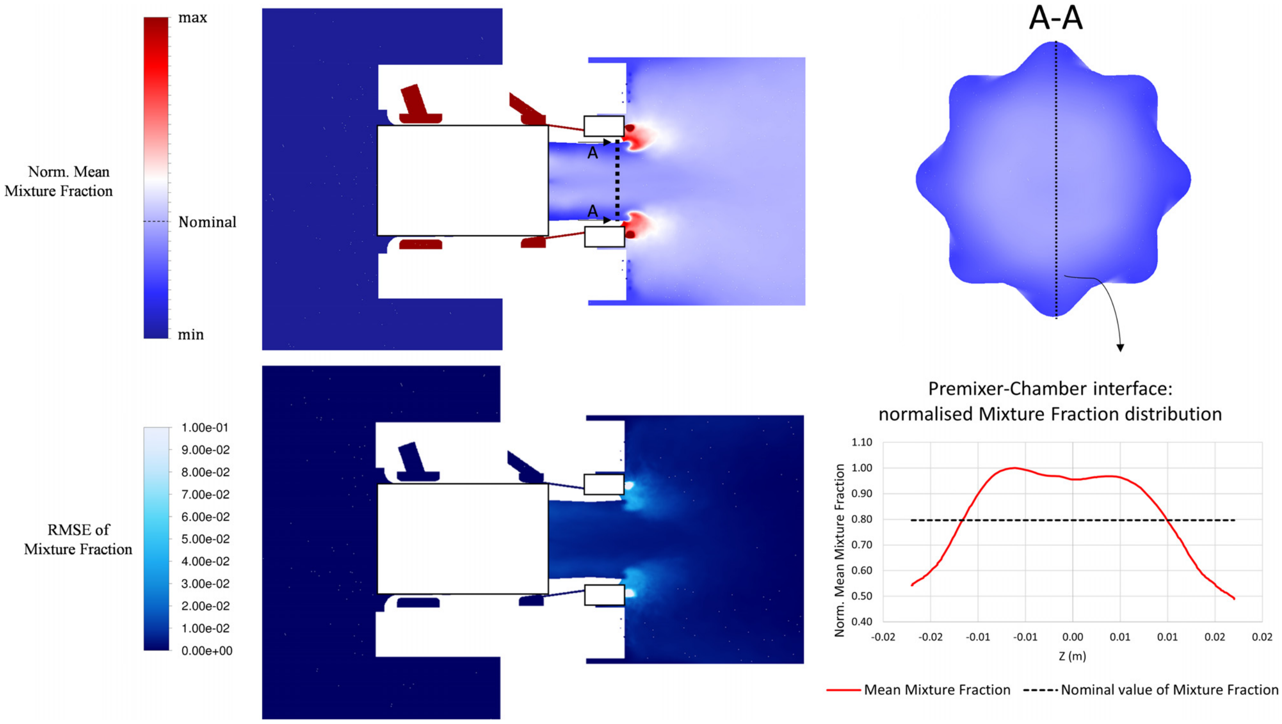

Fig. 8 Normalized time-averaged contours of mixture fraction on the $z-x$ plane of symmetry of the burner and a cross-sectional plane of the premixer (top). Additionally, a Z-axis distribution on the same plane and the root-mean-square error (RMSE) on the midplane are included for detailed analysis.

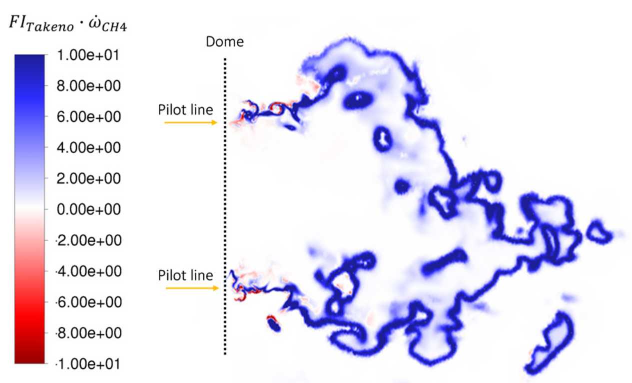

Fig. 9 Instantaneous contour of the normalized Takeno flame index on a longitudinal $z-x$ plane multiplied for the fuel consumption for better visualization. Regions with positive values are associated with a premixed regime, while zones with negative values correspond to a nonpremixed one.

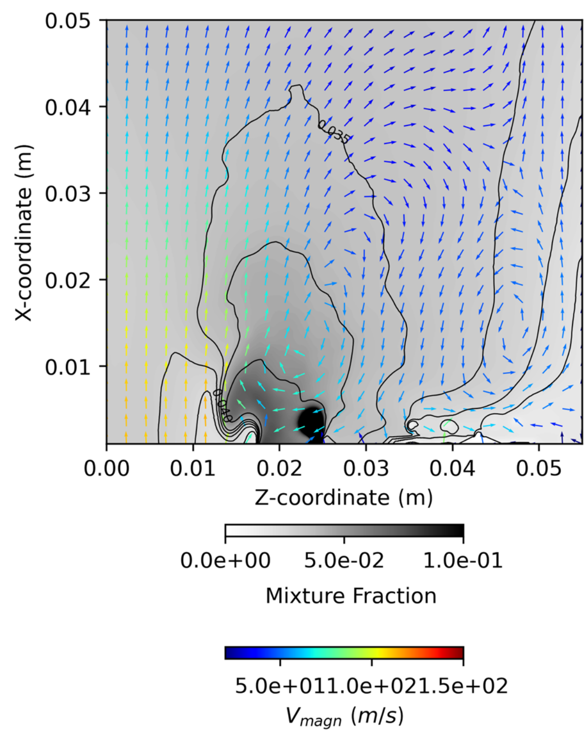

Fig. 10 Time-averaged mixture fraction field and velocity magnitude vector-plot on a longitudinal plane within the primary zone

mixture fraction and axial velocity fields on the $z-x$ plane of symmetry are depicted. The FGM model demonstrates a slightly richer mixture in the corner region. This observation is substantiated by the normalized mixture fraction distribution plot at 10 mm from the dome exit (Fig. 12), where the FGM model retains higher values at larger radial positions ($z > 0.3$). In contrast, the ATF model exhibits a tendency to slightly enrich the core region, as indicated by elevated Z values along the axis ($z = 0$). Beyond these distinctions, both models exhibit comparable behavior with no significant discrepancies.

Regarding axial velocity, the concordance between the two models is notably high. The FGM model displays a marginally higher axial velocity along the burner axis, especially at greater distances from the dome. To provide a thorough comparison, the corresponding RMS values are also presented, which further confirm the high degree of alignment between the models.

The observed discrepancies in heat-release fields between the FGM and ATF models have a direct impact on the thermal field.

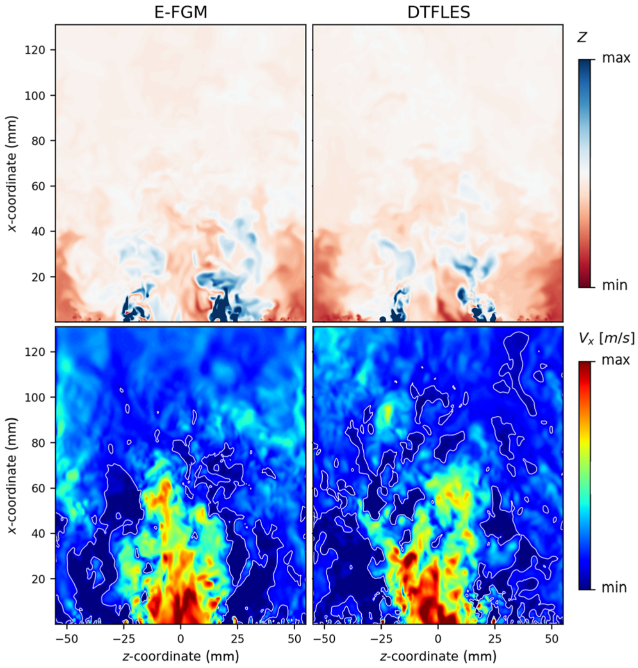

Fig. 11 Instantaneous mixture fraction (top) and axial-velocity (bottom) fields on the burner $z-x$ plane of symmetry for the FGM (left) and ATF (right) models

Figure 13 presents the contour plots of the time-average temperature in a longitudinal and a cross section inside the primary zone of the flame tube for both models. The FGM displays a central low-temperature region characterized by a more extended axial development, a feature clearly observable in the plots of Fig. 14. This is closely related to the FGM's inability to accurately capture the location of the heat-release peak. In contrast, the ATF, aligning with the experimental OH* images, positions the peak approximately 80 mm away from the chamber entrance, resulting in a shorter core low-temperature region. There are no significant differences in the cross-sectional temperature distributions within the primary zone, except for a slightly higher temperature affecting the corner region in the FGM simulations, consistent with the trends observed in mixture fraction. Generally, both models yield similar results in this specific region, aligning with findings from the heat-release contours.

5.3 Pollutant Emissions. As mentioned earlier, the primary goal of using high EGR percentages is to enhance the CO_2 content at the turbine outlet, maximizing the coupling efficiency between the gas turbine and the CCS unit. However, operating with high levels of EGR poses a critical challenge to flame stability due to the reduction of oxygen levels, potentially leading to increased CO and unburned hydrocarbons emissions associated with the decrease in overall flame reactivity. Monitoring CO is crucial as it provides insights into the flame stabilization mechanism. A sudden rise in CO concentration levels can serve as an early indicator of an impending blowout.

Exhaust gas recirculation is also well-known for effectively reducing NO_x emissions, particularly those resulting from the Zeldovich reaction mechanism, known as thermal NO_x. This is due to lower flame peak temperatures achieved by lowering the oxygen concentration within the combustion chamber, as well as through heat absorption. However, modern gas turbine burners are already capable of achieving single-digit NO_x emissions without the need for an EGR system to further decrease them.

This study specifically focuses on comparing the ATF and FGM models in predicting flame topology under given operating conditions. No optimizations were conducted to enhance the

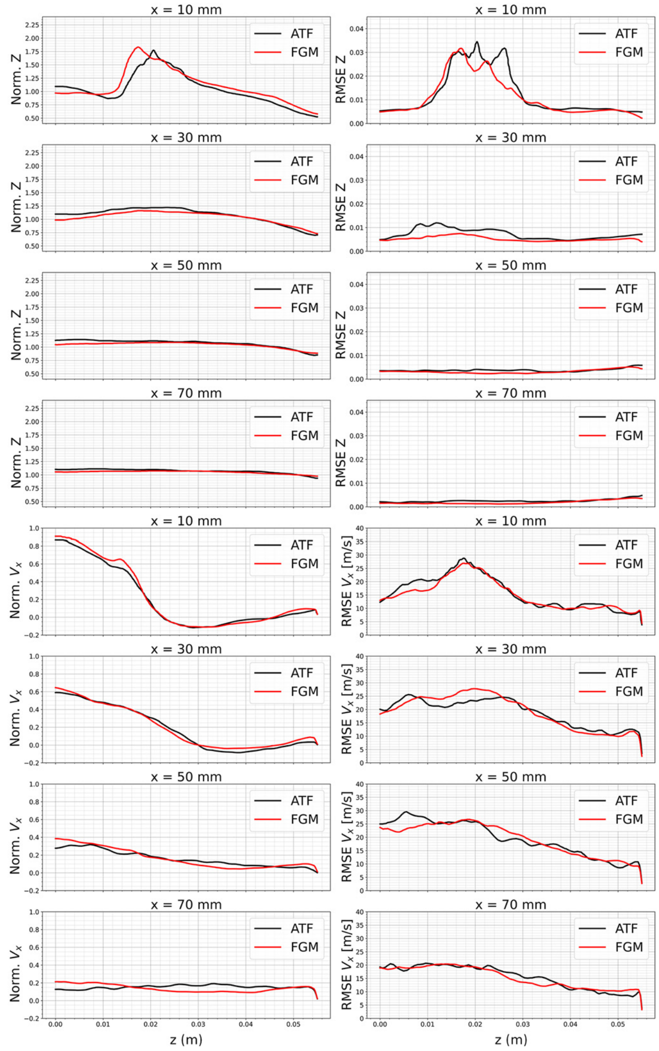

Fig. 12 Radial distributions of normalized time-averaged mixture fraction (top-left) and axial velocity (bottom-left) alongside their respective RMSE (right) at different axial coordinates: a comparison between ATF and FGM computed results

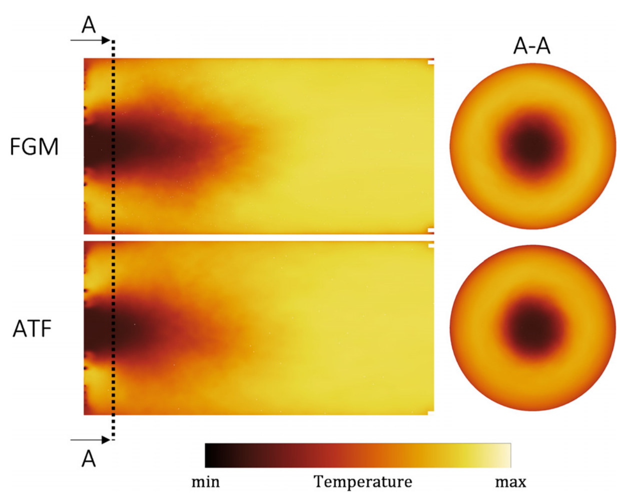

Fig. 13 Time-averaged temperature field on the $z-x$ plane of symmetry and a cross-sectional plane within the primary zone of the burner for the FGM (top) and ATF (bottom) models

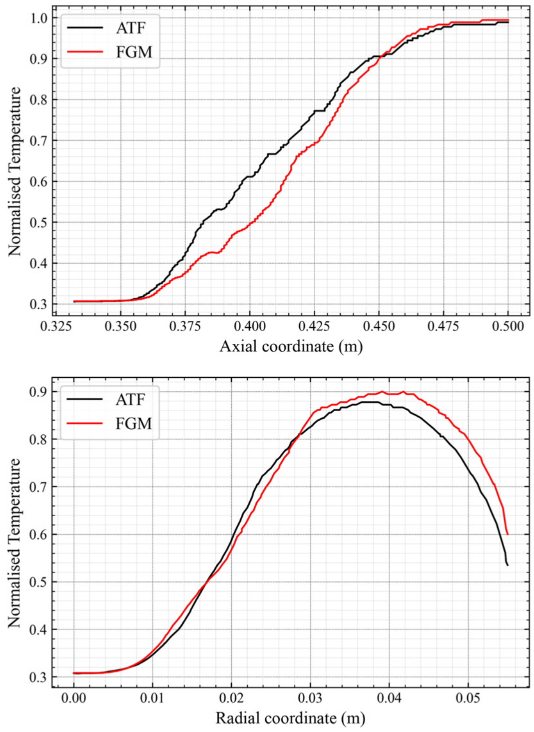

Fig. 14 Normalized time-averaged temperature distributions along the *x*-axis (top) and across the span of a cross-sectional plane (bottom) within the primary zone of the burner for both FGM and ATF models

models' capabilities in predicting pollutant emissions. Furthermore, as mentioned earlier, the ATF employs a 19-species reduced mechanism that does not include the NO_x species, as there was no specific interest in predicting them. Nevertheless, to offer a comprehensive view of the models' performance, a comparison of CO emissions is presented for both models against experimental data. Results from CFD were extracted on a plane located at the same position as the experimental extraction.

Figure 15 reports the normalized CO emissions for standard and CO_2-diluted air conditions from both experimental and numerical sides. As illustrated, both models are capable of capturing the increase in CO emissions, thus reflecting changes in the flame stabilization mechanism when switching from pure to diluted air conditions. However, as expected from a tabulated-chemistry approach, the FGM struggles to precisely compute the exact amount of CO emissions, especially when increasing the CO_2 content within the oxidizer, leading to about a 50% underestimation. On the other hand, the ATF can accurately predict the CO emissions in both the tested operating points, with just a 9% underestimation for the diluted air conditions.

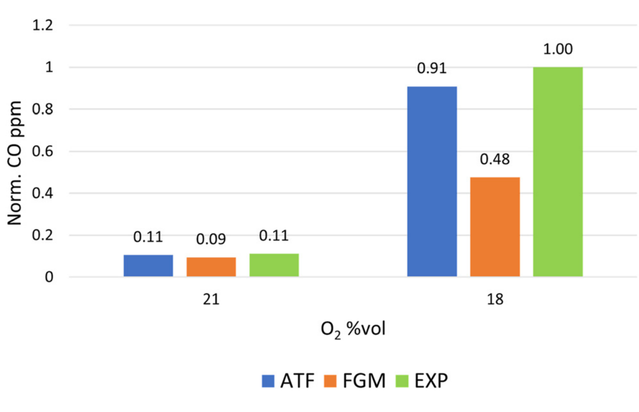

Fig. 15 Normalized CO emissions bar chart for standard and CO_2-diluted air conditions from both experimental and CFD sides

5.4 Computational Costs. All simulations showcased in this study were performed on a high-performance computing cluster comprising 20 multicore Intel® Xeon® Gold 6248 central processing unit (CPU) nodes. On this hardware, the computational cost for the entire simulation, including a preliminary Reynolds averaged Navier–Stokes calculation to generate a starting solution for the LES, along with the associated flushing and sampling stages, was estimated to be approximately 12,000 CPU hours for the FGM and 70,000 CPU hours for the ATF. The substantial difference in computational requirements arises from the ATF's need to address a transport equation for each species implicated in the reaction mechanism. In the applied skeletal version of the San Diego mechanism, this entails resolving 19 equations, resulting in a total of 23 equations for the ATF, as opposed to the eight equations for the FGM. Furthermore, the ATF employs a stiff chemistry solver to resolve the chemical reactions at the end of each time-step, thereby significantly increasing its overall computational cost. As a result, the computational expense associated with the ATF is approximately six times that of the FGM for the implemented numerical setup.

6 Conclusion

In this study, extended versions of the ATF and FGM models were utilized for high-fidelity CFD simulations in a lean-premixed burner by Baker Hughes, operating with significant CO_2 dilution in the oxidizer. The models' performances were compared in predicting flame topology using OH* chemiluminescence images from experiments as a benchmark. While both models showed analogous performance in a prior study under standard air conditions, minor discrepancies emerged under CO_2-diluted air, with the ATF showing slightly better performances over the FGM. The FGM failed to accurately predict the location of the heat-release peak, placing it solely near the pilots. In contrast, the ATF model was able to capture also the peak situated on the symmetry axis of the flame, far away from the dome, thus better aligning with experimental results. This disparity in the flame topology prediction between the two models directly influenced the thermal field, as the FGM exhibited an averaged lower temperature within the primary zone due to reduced heat release in that region. Despite the FGM's lower computational cost—about six times less than ATF—it effectively captured flame elongation and reduced heat release associated with lower oxygen concentration. Neither model, however, accurately predicted the local flame liftoff around the pilot jets. A sensitivity analysis of wall thermal boundaries, conducted to evaluate their influence on the flame stabilization mechanism, revealed no significant impact on the flame structure. Analysis of the mixing field revealed the cooling flow acting as a barrier between cooled recirculating gases and pilot jets, potentially explaining the low impact of wall heat losses on flame topology. These findings, along with experimental observations, suggest that local flame liftoff may be linked to a transient phase during ignition, a facet not simulated in this study, thus justifying the inability of both models to capture the phenomenon.

In conclusion, both models perform similarly under stable flame conditions, with small differences arising under critical conditions like those featuring high levels of CO_2 dilution, where near-blowout phenomena are essential to be captured. This is crucial during a burner design phase, where the dynamics of flame stabilization must be accurately captured in order to assess the combustor performance for different geometries and operating conditions. The combustion process in modern engines may not fully satisfy all flamelet assumptions, potentially compromising the accuracy of the FGM simulation results. Consequently, the ATF model, while more computationally demanding, provides slightly more accurate results.

Furthermore, without proper model customization, the FGM is not reliable for predicting CO emissions. In contrast, the ATF model shows consistency with experimental data for both standard and CO_2-diluted air conditions, making it the best choice for analyses focused on emission prediction.

On the other hand, the FGM model has demonstrated the capability to closely approximate the results of the more computationally intensive ATF model. The minor differences observed are insufficient to justify the significantly higher computational cost of the ATF, at least during preliminary geometry and design screening phases. Therefore, the FGM model emerges as the preferred choice for initial design analyses focused exclusively on flame topology and aerothermal fields.

Acknowledgment

The present research activity was carried out in the framework of TRANSITION (fuTure hydRogen Assisted gas turbiNeS for effective carbon capTure IntegratiON). The authors gratefully acknowledge this financial support.

Funding Data

- European Union's Horizon Europe research and Innovation programme (Grant Agreement No. 101069665).

Data Availability Statement

The datasets generated and supporting the findings of this article are obtainable from the corresponding author upon reasonable request.

Nomenclature

Roman Letters

a = strain rate (s^{-1})
c = FGM unnormalized reaction progress variable
D_{th} = thermal laminar flame thickness (m)
E = ATF model efficiency function
F = ATF model dynamic thickening factor
k = turbulent kinetic energy (m^2/s^2)
n = normal vector to the flame front
N_{thick} = number of points within the thickened flame front
P = static pressure (Pa)
$P(x)$ = PDF of the x-variable
S_l = laminar flame speed (m/s)
u = velocity x-component (m/s)
Y_i = elemental mass fraction of the i-species
Z = mixture fraction

Greek Symbols

Γ = extended-FR correction factor
Γ_k = extended-FR efficiency factor
Δx = mesh sizing (m)
δ_{ij} = Kronecker delta
κ = stretch (s^{-1})
ξ = Takeno flame index
σ_c = curvature (s^{-1})
ψ = extended-FR heat loss parameter
Ω = ATF model flame sensor
$\dot{\omega}_c$ = turbulent progress variable source term (s^{-1})

Subscripts and Superscripts

o = adiabatic unstrained condition
res = resolved quantity
sgs = subgrid scale modelled quantity
$\sim$ = Favre averaged quantity

Acronyms

ATF = artificially thickened flame
CFD = computational fluid dynamics
DTF = dynamic thickened flame model
EGR = exhaust gas recirculation
FGM = flamelet generated manifold
FR = finite rate
GT = gas turbine
HPC = high-performance computing
HTC = heat transfer coefficient
IRZ = inner recirculation zone
LES = large eddy simulation
LIRE = low-impact renewable energy
ORZ = outer recirculation zone
PDF = probability density function
PIV = particle image velocimetry
RMSE = root-mean-square error
THT = technology for high temperature
U.C. = University of California
UDF = user defined function
UHC = unburned hydrocarbons
WALE = wall-adapting local eddy-viscosity

References

[1] Pape-Salmon, A., Dogterom, J., Wieler, C., and Anielski, M., 2003, Low-Impact Renewable Energy Policy in Canada: Strengths, Gaps and a Path Forward, JSTOR, Pembina Institute, Calgary, AB, Canada, pp. 51–65.
[2] Tsiropoulos, I., Nijs, W., Tarvydas, D., and Castello, P. R., 2020, "Towards Net-Zero Emissions in the EU Energy System by 2050 - Insights From Scenarios in Line With the 2030 and 2050 Ambitions of the European Green," EN Publications Office of the European Union, Luxembourg, Report No. EUR 29981.
[3] Stefanizzi, M., Capurso, T., Filomeno, G., Marco, T., and Pascazio, G., 2021, "Recent Combustion Strategies in Gas Turbines for Propulsion and Power Generation Toward a Zero-Emissions Future: Fuels, Burners, and Combustion Techniques," Energies, **14**(20), p. 6694.
[4] Öberg, S., Odenberger, M., and Johnsson, F., 2022, "Exploring the Competitiveness of Hydrogen-Fueled Gas Turbines in Future Energy Systems," Int. J. Hydrogen Energy, **47**(1), pp. 624–644.
[5] Boot-Handford, M. E., Abanades, J. C., Anthony, E. J., Blunt, M. J., Brandani, S., Mac Dowell, N., Fernández, J. R., et al., 2014, "Carbon Capture and Storage Update," Energy Environ. Sci., **7**(1), pp. 130–189.
[6] Røkke, P. E., and Hustad, J. E., 2005, "Exhaust Gas Recirculation in Gas Turbines for Reduction of co_2 Emissions; Combustion Testing With Focus on Stability and Emissions," Int. J. Thermodyn., **8**, pp. 167–173.
[7] Herraiz, L., Diego, M., Bellas, J.-M., Finney, K., Pourkashanian, M., Runyon, J., Giles, A., Marsh, R., and Lucquiaud, M., 2021, "Selective Exhaust Gas Recycling in Gas Turbines With CO_2 Capture: A Comprehensive Technology Assessment," SSRN Electron. J., **1**, p. 16.
[8] Tanaka, Y., Nose, M., Nakao, M. T., Saitoh, K., and Ito, E., 2013, "Development of Low Nox Combustion System With EGR for 1700 °C-Class Gas Turbine," Mitsubishi Heavy Ind. Tech. Rev., **50**, pp. 1–6.
[9] Burnes, D., Saxena, P., and Dunn, P., 2020, "Study of Using Exhaust Gas Recirculation on a Gas Turbine for Carbon Capture," ASME Paper No. GT2020-16080.
[10] Li, H., Elkady, A. M., and Evulet, A. T., 2009, "Effect of Exhaust Gas Recirculation on Nox Formation in Premixed Combustion System," AIAA Paper No. 2009-226.
[11] Xie, M., Fu, J., Zhang, Y., Shu, J., Ma, Y., Liu, J., and Zeng, D., 2020, "Numerical Analysis on the Effects of CO_2 Dilution on the Laminar Burning Velocity of Premixed Methane/Air Flame With Elevated Initial Temperature and Pressure," Fuel, **264**, p. 116858.
[12] De Persis, S., Cabot, G., Pillier, L., Gökalp, I., and Boukhalfa, A. M., 2013, "Study of Lean Premixed Methane Combustion With CO2 Dilution Under Gas Turbine Conditions," Energy Fuels, **27**(2), pp. 1093–1103.
[13] Aniello, A., Laera, D., Marragou, S., Magnes, H., Selle, L., Schuller, T., and Poinsot, T., 2023, "Experimental and Numerical Investigation of Two Flame Stabilization Regimes Observed in a Dual Swirl h2-Air Coaxial Injector," Combust. Flame, **249**, p. 112595.
[14] Castellani, S., Meloni, R., Orsino, S., Ansari, N., Yadav, R., Bessette, D., Boxx, I., and Andreini, A., 2023, "High-Fidelity H2-CH4 Jet in Crossflow Modelling With a Flame Index-Controlled Artificially Thickened Flame Model," Int. J. Hydrogen Energy, **48**(90), pp. 35291–35304.
[15] Kazmouz, S., Haworth, D., Lillo, P., and Sick, V., 2022, "Extension of a Thickened Flame Model to Highly Stratified Combustion - Application to a Spark-Ignition Engine," Combust. Flame, **236**(02), p. 111798.
[16] Nassini, P. C., Pampaloni, D., Meloni, R., and Andreini, A., 2021, "Lean Blow-Out Prediction in an Industrial Gas Turbine Combustor Through a LES-Based CFD Analysis," Combust. Flame, **229**(07), p. 111391.
[17] Amerighi, M., Nassini, P., Andreini, A., Orsino, S., Verma, I., Yadav, R., and Patil, S., 2023, "Assessment of Flamelet Generated Manifold Approach With Inclusion of Stretch Effects of Pure Hydrogen Flames," ASME Paper No. GT2023-102651.
[18] Lemmi, G., Castellani, S., Nassini, P., Picchi, A., Galeotti, S., Becchi, R., Andreini, A., Babazzi, G., and Meloni, R., 2024, "FGM versus ATF: A Comparative LES Analysis in Predicting the Flame Characteristics of an Industrial Lean Premixed Burner for Gas Turbine Applications," Fuel Commun., **19**, p. 100117.
[19] Romano, S., Meloni, R., Riccio, G., Nassini, P. C., and Andreini, A., 2021, "Modeling of Natural Gas Composition Effect on Low Nox Burners Operation in Heavy Duty Gas Turbine," ASME J. Eng. Gas Turbines Power, **143**(3), p. 031018.
[20] Babazzi, G., Galeotti, S., Picchi, A., Becchi, R., Cerutti, M., and Andreini, A., 2024, "Combustion Diagnostics and Emissions Measurements of a Novel Low

NOx Burner for Industrial Gas Turbine Operated With CO_2 Diluted Methane/Air Mixtures," ASME J. Eng. Gas Turbines Power, **146**(7), p. 071007.
[21] Lilly, D. K., 1992, "A Proposed Modification of the Germano Subgrid-Scale Closure Method," Phys. Fluids A, **4**(3), pp. 633–635.
[22] Ducros, F., Franck, N., and Poinsot, T., 1998, "Wall-Adapting Local Eddy-Viscosity Models for Simulations in Complex Geometries," Numer. Methods Fluid Dyn. VI, **6**, p. 1.
[23] Ben-Nasr, O., Hadjadj, A., Chaudhuri, A., and Shadloo, M., 2017, "Assessment of Subgrid-Scale Modeling for Large-Eddy Simulation of a Spatially-Evolving Compressible Turbulent Boundary Layer," Comput. Fluids, **151**, pp. 144–158.
[24] Issa, R., 1986, "Solution of the Implicitly Discretised Fluid Flow Equations by Operator-Splitting," J. Comput. Phys., **62**(1), pp. 40–65.
[25] Issa, R., Gosman, A., and Watkins, A., 1986, "The Computation of Compressible and Incompressible Recirculating Flows by a Non-Iterative Implicit Scheme," J. Comput. Phys., **62**(1), pp. 66–82.
[26] Franzelli, B., 2011, "Impact of the Chemical Description on Direct Numerical Simulation and Large Eddy Simulation of Turbulent Combustion in Industrial Aero-Engines," Ph.D. thesis, Institut National Polytechnique de Toulouse – INPT, Toulouse, France.
[27] Colin, O., Ducros, F., Veynante, D., and Poinsot, T., 2000, "A Thickened Flame Model for Large Eddy Simulations of Turbulent Premixed Combustion," Phys. Fluids, **12**(7), pp. 1843–1863.
[28] Legier, J., Poinsot, T., and Veynante, D., 2000, "Dynamically Thickened Flame LES Model for Premixed and Non-Premixed Turbulent Combustion," Proceedings of the Summer Program, Stanford, CA, Vol. 1, pp. 157–168.
[29] Yamashita, H., Kushida, G., and Takeno, T., 1990, "A Numerical Study of the Transition of Jet Diffusion Flames," Proc.: Math. Phys. Sci., **431**(1882), pp. 301–314.
[30] Rosenberg, D. A., Allison, P. M., and Driscoll, J. F., 2015, "Flame Index and Its Statistical Properties Measured to Understand Partially Premixed Turbulent Combustion," Combust. Flame, **162**(7), pp. 2808–2822.
[31] University of California at San Diego, 2016, "Chemical-Kinetic Mechanisms for Combustion Applications, San Diego Mechanism web page, Mechanical and Aerospace Engineering (Combustion Research)," University of California at San Diego, San Diego, CA, accessed Sept. 17, 2024, https://web.eng.ucsd.edu/mae/groups/combustion/mechanism.html
[32] Peters, N., 1988, "Laminar Flamelet Concepts in Turbulent Combustion," Symp. (Int.) Combust., **21**(1), pp. 1231–1250.
[33] Hadadpour, A., Xu, S., Zhang, Y., Bai, X.-S., and Jangi, M., 2023, "An Extended FGM Model With Transported PDF for LES of Spray Combustion," Proc. Combust. Inst., **39**(4), pp. 4889–4898.
[34] Frenklach, M., Wang, H., Goldenberg, M., Smith, G., Golden, D., Bowman, C., Hanson, R., Gardiner, W., and Lissianski, V., 1995, "Gri-Mech: An Optimized Detailed Chemical Reaction Mechanism for Methane Combustion," Gas Research Institute Chicago, Chicago, IL, accessed Sept. 17, 2024, http://combustion.berkeley.edu/gri-mech/
[35] van Oijen, J., and Goey, P., 2000, "Modelling of Premixed Laminar Flames Using Flamelet-Generated Manifolds," Combust. Sci. Technol., **161**(1), pp. 113–137.
[36] Tay-Wo-Chong, L., Scarpato, A., and Polifke, W., 2017, "LES Combustion Model With Stretch and Heat Loss Effects for Prediction of Premix Flame Characteristics and Dynamics," ASME Paper No. GT2017-63357.